Matlab® toolbox for semi-automatic segmentation of the human nasal cavity based on active shape modeling

Reference:

Keustermans William, Huysmans Toon, Schmelzer Bert, Sijbers Jan, Dirckx Joris.- Matlab® toolbox for semi-automatic segmentation of the human nasal cavity based on active shape modeling
Computers in biology and medicine - ISSN 0010-4825 - 105(2019), p. 27-38
Full text (Publisher's DOI): https://doi.org/10.1016/J.COMPBIOMED.2018.12.008
To cite this reference: https://hdl.handle.net/10067/1559160151162165141

Matlab® toolbox for semi-automatic segmentation of the human nasal cavity based on active shape modeling

William Keustermans[a,*], Toon Huysmans[b,1], Bert Schmelzer[c], Jan Sijbers[b], Joris JJ Dirckx[a]

[a]Physics department, University of Antwerp, Laboratory of Biophysics and Biomedical Physics, Groenenborgerlaan 171, 2020 Antwerp, Belgium

[b]Physics department, University of Antwerp, Imec-Vision Lab, Universiteitsplein 1, 2610 Antwerp, Belgium

[c]ENT department, ZNA Middelheim hospital, Lindendreef 1, 2020 Antwerp, Belgium

*Corresponding author:

William Keustermans, U.339
Groenenborgerlaan 171
2020 Antwerpen
Belgium

william.keustermans@uantwerpen.be

Abstract

The nose is a complex and important organ with a multitude of functions. Computational fluid dynamics (CFD) has been shown to be a valuable tool to obtain a better understanding of the functioning of the nose. CFD simulations require a surface geometry, which is constructed from tomographic data. This can be a very time-consuming task when one chooses to exclude the sinuses from the simulation domain, which in general keeps the size of the CFD model more manageable. In this work, an approach for the semi-automatic construction of the human nasal cavity is presented. In the first part, limited manual interaction is needed to create a coarse surface model. In the next part, this result is further refined based on the combination of active shape modeling with elastic surface deformation. The different steps are bundled in a Matlab toolbox with a graphical interface which guides the user. This interface allows easy manipulation of the data during intermediate steps, and also allows manual adjustments of the reconstructed nasal surface at the end. Two results are shown, and the approach and its precision are discussed. These results demonstrated that the

---

[1] Present address: Faculty of Industrial Design Engineering, TU Delft, Landbergstraat 15, 2628 CE Delft, The Netherlands

followed approach can be used for the semi-automatic segmentation of a human nasal cavity from tomographic data, substantially reducing the amount of operator time.

Keywords

nose, statistical shape model, cylindrical parametrization, active shape model, elastic surface, graphical user interface

1. Introduction

The nose is an important organ which has multiple functions including olfaction, filtering, heating and humidifying the inhaled air. People who suffer from nasal function impairment can have a reduced quality of life (Rhee et al., 2003). Computational fluid dynamics (CFD) has been shown to be a valuable tool to study the functioning of the nose. Over the last 25 years, this technique has been increasingly used in several studies to predict airflow throughout the nasal cavity based on three-dimensional models derived from computed tomography (CT) or magnetic resonance imaging (MRI) data (Keyhani et al., 1995, 1997; Subramaniam et al., 1998; Grant et al., 2004; Wexler et al., 2005; Garcia et al., 2007; Doorly et al., 2008; Leong et al., 2010, Rhee et al., 2011, Lindemann et al., 2013; Frank-Ito et al., 2014; Inthavong et al., 2017). CFD was used to understand the normal and pathological airflow physiology (Garcia et al., 2007; Wen et al., 2008; Di et al., 2013) by determining nasal resistance and local airflow effects of inferior turbinate reduction (Wexler et al., 2005) septal perforation (Grant et al., 2004; Lindemann et al., 2013), septal deviation (Ozlugedik et al., 2008; Garcia et al., 2009), and radical sinus surgery (Lindemann et al., 2005). CFD can also be coupled to different physical laws, such as particle deposition and heating loss. Particle deposition in the nose depends on the airflow and is important for understanding the cleansing function of the nose and for drug delivery (Inthavong et al., 2006; Schroeter et al., 2006; Kimbell et al., 2007; Karakosta et al., 2015).

CFD could also add value as an objective tool for pre-operative assessment in the ear-nose-throat (ENT) department. A major obstacle for this field of application is the time needed to manually construct a surface geometry of the nose from tomographic data (Tingelhoff et al., 2007). During stable respiration, the flow rate through the sinuses is only a fraction of that through the nose (Xiong et al., 2008), while the simulation domain is considerably larger and more complex when the sinuses are included. Both complexity and size of the domain have a major effect on the simulation time. When investigating non-sinus related pathologies, one could therefore choose to exclude the sinuses from the nasal cavity to simplify the computational models.

Methods exist which are capable of producing adequate segmentations of the upper respiratory tract. Last et al. (2010) presented a model-driven approach based on parametric level set for the segmentation of the nasal cavity and paranasal sinus boundaries. Their aim was to extract the border between these regions of interest and the rest of the head, and they evaluated their method on 2D slices. The borders indicating the region of interest are however not suited for CFD calculations. In Bui et al. (2015), a multi-step level set segmentation procedure was created to construct the nasal cavity with paranasal sinuses from cone-beam computed tomography (CBCT) scans of the head. Other existing methods are based on thresholding (Dastidar et al., 1999; Shi et al., 2006; El et al., 2011; Iwasaki et al., 2011) and region growing (Tingelhoff et al., 2007; Seo et al., 2010). An algorithm for the segmentation of the nasal cavity and pharyngeal airway in CBCT images has been presented in Alsufyani et al. (2016). In that work, localized threshold decomposition gradient segmentation (LEDGES) was used to locally select the threshold that indicates the region of interest. A free upper respiratory tract 3D model reconstruction software, called NASAL-Geom, was described in Cercos-Pita et al. (2018). This software was optimized for producing 3D nasal geometries from CT scans. Burgos et al. (2017) developed a novel algorithm to build the 3D geometry from segmentation images, as an alternative to the Marching cubes algorithm (Lorensen and Cline, 1987). Based on their method they presented a model of the nose including the sinuses.

The majority of the above methods are either restricted to a single image modality (cone-beam CT) or they are not designed to separate the nasal cavity from the sinuses, which can be desirable for

CFD calculations. In this paper another approach is followed that is not restricted by the image modality and that can separate the sinuses from the nasal cavity. This approach was also followed by Huang et al. (2016). However, in their work the statistical shape model (SSM) was constructed using level sets, which have some known weaknesses.

In this work, the statistical shape model was built using point correspondences. The manual step, that is, the total segmentation process or only a refinement step, is replaced by a step based on active shape modeling (ASM). Replacing the manual step substantially reduces the amount of user interaction. A toolbox is created in Matlab (MathWorks, Natick, MA, USA) to guide the user through the whole segmentation process.

2. Methods

Our proposed Matlab toolbox is interface-oriented and divided in three parts. In the first part, the tomographic data is preprocessed by creating a binary 3D matrix, which is the coarse segmentation. In what follows, this step will be referred to as the 'masking' step. In the second step, the coarse result is further refined using a high quality SSM of the nasal cavity in combination with the ASM algorithm (Cootes et al., 1995) and an elastic surface deformation step (Amberg et al., 2007). This will be referred to as the 'geometry' step. As a final operation, the result is transformed back into a binary matrix, and the user has the opportunity to make some manual adjustments if needed. This step is called the 'inspector' step. Figures 1 and 2 show a general overview of the user interface and the different tabs that constitute the toolbox.

2.1 Defining the region of interest

After the CT data is loaded into the toolbox, the first step is to construct a region of interest by defining interval limits for the grayscales (figure 3). Grayscales within the interval are set to one – in this case the air cavities – and the other regions like soft tissue and bone are set to zero. Before applying these limits, a transversal closing operation has to be defined anteriorly on the nostrils and posteriorly on the floor of the turbinates, where the nasopharynx (NP) starts. During this closing step, the voxels of one CT slice in a user defined region are set to a value higher than the maximum grayscale value in the CT scan. Those voxels form a boundary when the grayscale limits are applied, making this a simple but effective method to close a 3D region of interest. The closing operation is used for two reasons. Closing the nostrils makes it possible to separate air surrounding the head from the air filled cavities inside the head; as the interest goes out to the latter, only voxels corresponding to those cavities should be set to one. The second closing operation is related to the shape of the SSM used for the segmentation refinement. How exactly the SSM is defined and the purpose of the closing operation will be explained in detail in section 2.3.1. For the first closing operation there is the option to let an automated process close the nostrils. This process consists of a combination of morphological operations and was tested on a set of CT scans. For most scans the automated process gave good results, but because of considerable variation in the nostrils' shape and orientation, it is not fully robust, so a manual user intervention can be used as a second option. After the procedure, the voxels’ indices of the NP and throat are saved by clicking on one of the voxels belonging to those regions. These voxels will be added to the segmentation result when the coarse and fine segmentation steps are done (section 2.4). The closing operation together with the limits for the grayscales defines the region of interest. The voxels within the region of interest are set to one and those outside of it (including the boundaries used for closing) to zero.

2.2 Coarse segmentation: excluding the sinuses

2.2.1 Watershed procedure

Next, a watershed operation is applied on this binary matrix. More precisely, an Euclidean distance transform is carried out on the complement of the binary matrix. Next, an H-minima transformation is applied on the negative of this distance transform. This transformation suppresses all minima smaller than a defined value. Otherwise, the procedure would produce a large amount of sheds basins. The result forms the input for the watershed algorithm. This operation separates already large parts of the sinuses from the real region of interest, i.e., the nasal cavity. Subsequently, the user can click on the parts that have to be deleted (figure 4).

2.2.2 Morphological operations

The basins resulting from the watershed algorithm are a fraction smaller in volume than the original region, because of the definition of the watersheds. Therefore, the user has the possibility to grow or shrink the indicated regions (sinuses) before subtracting them from the region of interest, and to remove any small clusters of voxels (called islands) that are formed by this operation (figure 5). In figure 6 an example is shown of a surface model obtained after applying this procedure. This surface was calculated from the binary data. The latter is the format in which it is used in the segmentation refinement (section 2.3). It is clear that almost all sinuses are removed, but the current geometry still contains some unwanted parts. These have to be removed when the geometry is going to be used as the simulation domain in CFD calculations. The further refinement of this result is explained in the following section.

2.3 Segmentation refinement using ASM and elastic surface deformations

2.3.1 Statistical shape model of the nasal cavity

In the following, a brief explanation is given on the construction of the SSM. The morphological information contained in this nasal SSM is used by the ASM during the fitting process, as described later on.

Data were obtained from 46 patients with different nasal or sinus related complaints, where the treating ENT physician requested a CT scan. The spatial resolution of the scans ranges from 250 µm to 430 µm perpendicular to the axial direction, and from 250 µm to 600 µm in the axial direction. From each CT scan a geometrical surface model was built by segmentation using Amira 6.0.1 (FEI, Hillsboro, OR, USA). Grayscale thresholding was applied to determine the nasal passages. The nasal cavity and sinuses were manually separated by a single operator for all CT data to avoid inter-operator generated variations between segmentations. From now on, these manual segmentation results will be called labels.

To be able to create a SSM, all training meshes have to contain the same amount of vertices, which have to be located at the same anatomical position. Surface meshes for which this condition holds are said to ‘correspond’. The algorithm used for this correspondence step is discussed further on, and demands that all training surfaces have topology genus-0. Holes in the labels were therefore filled. The end of the post-nasal region is different for all nasal shapes, because the field of view varies between scans. When not corrected for, a large non-anatomical variation would be introduced in the shape model, as the extent over which the scan was taken affects the length of the post-nasal region. For this reason the labels cannot be used as is. To create matching post-nasal regions, the labels were cut perpendicular to the axial direction at the floor of the inferior turbinates.

Next, a triangulated surface geometry is built from the generated labels using the Marching Cubes Algorithm (Lorensen and Cline, 1987), which is smoothed in a following step. With smoothing one should always try to minimize potential surface shrinkage. In Amira 6.0.1 a surface smoothing algorithm is implemented based on Taubin (1995), called “Curve and surface smoothing without shrinkage”. For all shapes a tiny hole was cut in both nostrils at the same anatomical position, hereby fulfilling the final condition of the correspondence algorithm. Using Paraview 5.4.0 (Kitware Inc., NY, USA), mirrored versions of the nasal cavity shapes were created. Because the number of shapes is doubled, the amount of variation present in the shape model will be larger.

The next step in building the SSM is the surface correspondence, which results in a dense one-to-one map between the training surfaces. To guarantee a uniform surface sampling, the correspondence method of Huysmans et al. (2010) was modified. The method consists of four main steps. Each surface was cylindrically parameterized in the first step, using the method of Huysmans et al. (2004), supplying the vertices of each surface with coordinates that define a low-distortion one-to-one mapping between each surface and the cylinder. The small holes in the nostrils made earlier, correspond to the two boundary ends of the cylinder. Between any two nasal cavities in the training set, a correspondence can be derived by composition of these maps. In the second step, a rigid transformation of the surfaces is done and the parameterizations were rotated for optimal alignment following the minimum description length (MDL) objective of Davies et al. (2002). MDL, a measure based on the minimum description length principle, encodes the training surfaces in a message using the PCA model obtained with the correspondence. The combined length of the message with the encoded model gives the quality of the correspondence. There is a trade-off between goodness-of-fit and the complexity of the model. The MDL measure introduced by Thodberg (2003) was used in this work, which is a function of the shape mode variances. The correspondences were further fine-tuned in the third step, by non-rigid deformations in the parametric domain for each of the surfaces. Optimality was again measured with the MDL objective. The optimal parameterizations were used in the final step to generate a vertex correspondence for the training set, such that each shape is represented with a fixed number of landmarks. Across the training set, these landmarks are at corresponding anatomical locations.

As a result, each nasal shape is represented by a set of points distributed over the boundary. Each of them is located at the same anatomical location on all shapes. From the 92 corresponded nasal shapes a SSM was built by applying principal component analysis (PCA) on the vertices of the surfaces. A nasal shape was considered to be independent of position and orientation, but not of scale. Procrustes analysis was used to determine the optimal poses. During Procrustes analysis, the entire training set is aligned with a reference shape. In the first iteration, a shape from the set is chosen as reference shape. From then on, the average shape calculated in the previous iteration is used as reference. During the analysis, translational differences were removed by aligning the centroid of each training shape, and the rotation matrix between each training shape and the reference shape was calculated using quaternions. The PCA delivered an average nasal shape $\bar{x}$ and an orthogonal set of eigenvectors ϕ^k representing the shape variations. The average nasal shape is symmetrical because both the original and mirrored versions are included in the dataset. New and existing nasal shapes can be described as the sum of the average nasal cavity and a linear combination of those shape variations, also called shape modes (figure 7). Some of the eigenvectors will only explain a small fraction of the total variation captured by the shape model, and they potentially describe variation caused by noise in the training data. The dimensionality of the shape space can therefore be further reduced, for example by defining a cut-off value for the cumulative variance.

2.3.2 Active shape model

The active shape modeling algorithm uses these shape modes to deform the average nasal shape, in combination with an appearance model which steers these deformations. For more information, the reader is referred to Cootes et al. (1995). In that work the appearance model was built from binary data obtained from the manual segmentations. The so called profiles g_{s_i} (where i denotes a landmark) with length $2l + 1$ are sampled perpendicular to the boundary of the nasal shape (l in both directions plus the vertex position). Doing this for the whole training data set leads to a set of samples $\{g_{s_i}\}$ for every model point. An average sample line g_{a_i} and covariance matrix S_i can then be calculated for each landmark. During the fitting process, the inverse of S_i is used to calculate the so called Mahalanobis distance D, defined as: $D_i = \sqrt{(g_{s_i} - g_{a_i})' S_i^{-1} (g_{s_i} - g_{a_i})}$ (eq. 1)

Minimizing D_i maximizes the probability that g_{s_i} is drawn from the distribution with average g_{a_i} and covariance matrix S_i. To ensure non-singularity of the covariance matrices, random noise with a range 1000 times smaller the range of the covariance matrices is added to the sampled training data. This is done only for the calculation of S_i^{-1}. The average sample lines g_{a_i} and inverse covariance matrices S_i^{-1} form the appearance model. Appearance models with different profile lengths can be calculated in advance of the fitting procedure, creating a database. During the fitting procedure the user can choose from this database of models.

The procedure starts by initializing the average shape $\bar{x}$ of the statistical shape model. For active shape modeling, this initialization of the symmetrical average nasal shape is an important condition to ensure a qualitative outcome. It becomes extremely difficult to ensure a good fit when the initialization of a complex model like the human nose is far from the optimum at the beginning, especially within a reasonable time frame. From the binary result obtained in the coarse segmentation, a centroid is calculated and $\bar{x}$ is translated from the origin to this centroid. The user interface allows manual adjustments, that is, translations t_x, t_y, t_z and rotations $\theta_x, \theta_y, \theta_z$, to optimize this initial pose with direct visual feedback.

In a next step, the appearance model can be loaded into the toolbox. At his point, fit parameters have to be set. More information on these settings can be found in section 2.3.4. While fitting, the appearance model steers the deformations because it is used in combination with the profiles sampled perpendicular to the surface. This is done in the following way: for every vertex of the nasal shape, a sample line of length $2L+1$ is defined perpendicular to the nasal shape. At each position of this sample line, a profile of length $2l+1$ is sampled.

The goodness of fit can be tested using D_i for the different positions, and the one with the lowest value indicates the new optimal position for the vertex at that iteration. This process is done for every landmark at each iteration step j. The vertices are translated to their best match, which deforms the nasal shape x. The shape parameters b^k describing x are calculated, and in a next step this shape is projected back to the known shape space by limiting the parameters b^k to plus or minus n (with $n \leq 3$) times the standard deviation σ^k. b and σ are both vectors with size equal to the number of shape modes. Repeating these steps represents the basic active shape modeling algorithm, and can be mathematically expressed as:

$$x_j^i \xrightarrow{\min D_i} x_j^{i\prime}$$

(eq. 2)

$$b_j^k = \phi^{k^{-1}}\left(\tilde{x}_j^{i\prime} - \overline{x^{\iota}}\right)$$

(eq.3)

$$-n\sigma^k \leq b_j^k \leq n\sigma^k \xrightarrow{yields} b_{j+1}^k$$

(eq. 4)

$$\tilde{x}_{j+1}^i = \overline{x^{\iota}} + \phi^k b_{j+1}^k$$

(eq. 5)

$$\tilde{x}_{j+1}^i \xrightarrow{add\,pose} x_{j+1}^i$$

(eq. 6)

where $\tilde{x}$ denotes the shape without pose (so after the Procrustes alignment of x with $\bar{x}$). When the projection to the shape space is done and b_j^k is calculated, pose is added back to the nasal shape, giving x_{j+1}^i, which forms the start of a new iteration. The choice for the value of n depends on whether the projection to the known shape space produces realistic shapes (shapes with no intersecting faces). It can also be set to a value lower than 3.

The procedure explained above is extremely sensitive to bad matches based on the Mahalanobis distance. A landmark that is shifted to a bad location, and hence becomes an outlier, will have a considerable impact on the value of the b-parameters, because b_j^k is calculated using all landmarks. One outlier can have a big impact on the projected shape, causing it to diverge away from the shape of interest. For example, when all positions along the sample line have high Mahalanobis distances, the algorithm would just take the one with the least high value. As a consequence, the matching point can be way off. To avoid this, two criteria were added to the algorithm: $D_i < D_c$ (eq. 7) and $D_{along\ sample\ line} \neq cst$ (eq. 8). Equation 7 expresses that landmarks with a Mahalanobis distance higher than a chosen critical value are not used in the projection step. Equation 8 states that landmarks with a constant Mahalanobis distance along the entire sample line are also excluded from the projection step. For these landmarks no true optimal position was found because only voxels corresponding to air are sampled. Only the landmarks that meet these two conditions are used during the projection. In the beginning this can be a small fraction of the total number of landmarks. The number of landmark vertices that contribute changes during the fitting process, as shape deformations will cause a vertex to have a new sample line. Another way is to alter the critical value D_c during subsequent iterations. In the current setup, this is done indirectly by using a user defined percentage of points that should contribute, and by calculating D_c by ranking the vertices by their value of D.

Resampling the appearance data allows bigger landmark translations and can therefore accelerate the fitting. However, in the current implementation this was deemed unnecessary because of the thorough initialization step executed at the start of the fitting process.

2.3.3 The nasal cavity as an elastic surface

It is impossible for a shape model based on 46 training shapes and their 46 mirrored counterparts to already capture the full scale of nasal shape variation that exists. On the other hand, variation that is already captured should be exploited as good as possible during fitting. This can only be done when the correspondence between the shape model and the new, to be fitted, nose is optimal. Only then the shape model will fully be able to determine if the shape falls within the known shape space. If during fitting the model gets stuck in a local minimum and the projection step is not able solve this, the model will not fit optimally to the new nasal shape. A mechanism is needed to correct this. Otherwise, the fitted shape has a high probability to wrongly fall outside of the known shape space.

The method used in this work models the nose as an elastic surface, and is based on Amberg et al. (2007). Between two consecutive iterations, the elastic surface is allowed to stretch. The amount of stretch depends on the stiffness of the surface, which lowers with increasing number of iterations. In the beginning the surface is quite stiff, such that the surface can only undergo a global scaling. Further on in the fitting process, the surface becomes less stiff and each landmark can move more and more independently. A landmark position is represented using homogeneous coordinates $v_i = [x\ y\ z\ 1]^T$, and with each of them an affine 3 x 4 transformation matrix X_i is associated. Each landmark is aiming for the optimal position with coordinate u_i as determined by the appearance model. This leads to a 4n x 3 matrix X for the whole nasal shape, with n the number of landmarks. From a mathematical standpoint, the minimum of the energy function $E_{total}(X) = E_d(X) + \alpha E_s(X)$ (eq. 9) has to be found. E_d and E_s are respectively the distance and stiffness term, and α the stiffness factor. E_d is minimized by minimizing the distance between the current position of the landmarks and their optimal positions. This means that during the elastic step, the deformation of the surface is, just like during the ASM step, based on vertex translations along the surface normals. Using the Frobenius norm $\|.\|_F$, the distance term can be written as (Amberg et al., 2007):

$$E_d(X) = \sum_{v_i} w_i \| X_i v_i - u_i \|^2$$

$$= \| W(DX - U) \|_F^2$$

(eq. 10)

W, D and U are defined by:

$$W = \begin{bmatrix} w_1 & & & \\ & w_2 & & \\ & & \ddots & \\ & & & w_n \end{bmatrix}, \quad D = \begin{bmatrix} v_1^T & & & \\ & v_2^T & & \\ & & \ddots & \\ & & & v_n^T \end{bmatrix}, \quad U = \begin{bmatrix} u_1 \\ u_2 \\ \vdots \\ u_n \end{bmatrix}$$

(eq. 11)

The diagonal entries w_i of the matrix W are weights associated with each vertex pair (v_i, u_i). In this work binary weights were used, meaning that the vertex pair either contributes or does not contribute to the energy term. The value of these weights is directly linked to the outlier detection in the active shape modeling step. Landmarks were seen as outliers when no new optimal position that satisfies equation 7 and 8 could be found. Likewise, the weight w_i of these outliers is set to zero during the elastic step.

The stiffness term E_s penalizes differences between the transformation matrices of neighboring landmarks. This term is minimized when all landmarks undergo the same transformation X_i. The stiffness term can be expressed as (Amberg et al., 2007): $E_s(X) = \|(M \otimes G)X\|_F{}^2$ (eq. 12). Where $\otimes$ denotes the Kronecker product and G is a diagonal matrix given by:

$$G = \begin{bmatrix} 1 & & & \\ & 1 & & \\ & & 1 & \\ & & & \gamma \end{bmatrix}$$

(eq. 13)

γ is a weighting factor for differences in the skew and rotational part of the deformation versus differences in the translational part of the deformation. The value of γ in this work is set to 1 for all executed fitting procedures (in the following also called runs). M is the so called node-arc incidence matrix, for more information the reader is referred to Jeter (1986). A row in M corresponds to one edge of the nasal shape, and a column to one vertex. M is constructed by numbering all edges and vertices of the surface model and directing the edges from the lower numbered to the higher numbered vertex. Matrix M is a sparse matrix, where an entry $M_{edge,vertex}$ is only nonzero if that specific edge connects the vertex to another neighboring vertex. The entry will be plus or minus 1 depending on whether the edge leaves from or arrives at the vertex, respectively.

The factor α gives a weight to this stiffness term, and in this way acts as virtual stiffness factor. In the beginning when α is high, the first term of equation 9 becomes negligible. The determination of the lower boundary for α requires trial and error, and is specific to each problem. In case of the nasal cavity, a very unsmooth surface (with possible local peaks) is unwanted, therefore α_n always remains larger than 1. In practice, a value of 4 seemed suited.

Using equation 10 and 12, the total energy term can be written as:

$$E_{total}(X) = \left\| \begin{bmatrix} \alpha M \otimes G \\ WD \end{bmatrix} X - \begin{bmatrix} 0 \\ WU \end{bmatrix} \right\|_F^2$$

$$E_{total}(X) = \| AX - B \|_F^2$$

(eq. 14)

$E(X)$ is a quadratic function and can be minimized directly. It reaches its minimum for $X = (A^T A)^{-1} A^T B$. When X is known, DX deforms the shape obtained from the active shape modeling step, exactly minimizing E_{total}. The resulting shape is the input for the next ASM iteration.

2.3.4 Geometry tab settings

Figure 2 includes a detailed view of the 'geometry' tab. At the top, there are two lines right below the option to manually change the centroid. One contains the directory of the shape model, and the other contains the database directory of the appearance model. The appearance models are named in a specific way, such that when one is loaded the number of appearance scales and the length of the profile lines used to generate the ASM are automatically known and set. At this moment, the half-length L of the sample line, the percentages of initial points, and the number of iterations for every percentage level have to be defined.

Two final inputs concerning the elastic surface step need to be entered: the weight γ and the boundaries (α_n, α_1) of the stiffness factor α_j. With each iteration j, the stiffness factor decreases from the maximum value α_1 to the minimum value α_n following:

$$\alpha_j = \alpha_1 - \left[\left(\frac{(j-1).\sqrt{\alpha_1 - \alpha_n}}{n-1}\right)^2\right]$$

(eq. 15)

Where n denotes the total number of iterations. Equation 15 describes a quadratically decreasing function and was found suitable by trial and error.

During fitting, three parameters are calculated and shown (the two latter also plotted): the current iteration number, the percentage of points used (POPU) and the percentage of points satisfying the sampling criterion (POPSSC). The POPU graph will converge more and more to the POPSSC graph during fitting, where the POPSCC always forms the upper limit for the POPU. At the end though, they do not have to coincide.

2.4 Voxelizing the geometry

As described in the section above, the active shape modeling is alternated with an elastic deformation step. When the amount of iterations defined by the user is reached, the algorithm stops and delivers the nasal shape in the form of a surface mesh (vertices, faces). As a next step, the user should be able to compare the segmentation result with the original tomographic data, allowing a visual estimate of the goodness of fit (just like this is the case when manually segmenting a nose). When a region is segmented suboptimally, it should also be straightforward to make changes to the existing segmentation. A surface mesh is not appropriate for these steps. The mesh was therefore voxelized, making use of the Matlab file exchange package called “Mesh voxelization” (Mesh voxelization, 2013). Voxelization sets all voxels inside the surface to one and the ones outside of it to zero. The details of the applied technique do not fall in the scope of this work, and in the following the underlying idea is only briefly discussed.

Using the vertices of the surface mesh, the bounding box dimensions can be calculated, and this box can be subdivided into voxels. One defines rays starting at the bottom face of the bounding box, which propagate perpendicular to the face. For each ray, the coordinates (x_{int}, y_{int}) of the intersections with the surface mesh can be listed. In a next step, the z-coordinate of these intersections can be calculated using the equation for a plane in 3D-space: $Ax_{int} + By_{int} + Cz_{int} + D = 0$ (eq. 16). When all intersections $(x_{int}, y_{int}, z_{int})$ for each ray are known, the voxels in between are set to one, while the others remain zero, and a binary matrix is obtained from the nasal surface mesh.

2.4.1 Inspecting the result

It is also at this moment that the voxels of the NP and throat are added to this binary matrix. These voxels were removed in the very beginning using the closing operation. In the following, the voxelized nasal surface mesh together with the voxels of the NP and throat will be called the segmentation matrix.

The inspection of the segmentation result is made possible by combining it with the original CT data and the original binary matrix. A first way is to impose the segmentation result on the original CT data. Another possibility is to check which voxel has a higher or lower value in the segmentation matrix compared to the corresponding voxel in the binary mask. This allows making a visual map of the goodness of fit (figure 8), and changes can be made accordingly (section 2.4.2). The map is defined as follows:

$$Voxel_{Segm} > Voxel_{CT} \ \rightarrow \ blue$$

$$Voxel_{segm} > Voxel_{binary} \ \rightarrow \ red$$

$$Voxel_{segm} < Voxel_{binary} \ \rightarrow \ green$$

The blue color indicates voxels belonging to the segmentation result which are potentially correct. No distinction is made between a voxel positioned at a sinus or in the nasal cavity. Green indicates voxels with a value of one in the original binary matrix and zero in the segmentation result. Ideally, all voxels and only the voxels of the sinuses are green, meaning that the fitting procedure would have completely excluded the sinuses. Voxels which have a value of one in the segmentation result and zero in the binary matrix are colored in red. Ideally, no voxel should be red, because this indicates that the active shape model segmented a voxel that does not belong to the nasal cavity. However, there are two exceptions. The surface correspondence step placed a restriction on the topology of the shapes. Because of this, it is expected that the active shape model will for example ignore a nasal septum perforation. This can easily be manually adjusted. The second exception concerns the voxels of the NP and throat that were removed during the closing step. As a logical consequence, these voxels will be colored in red. During inspection it can also be that loose red voxels are visible, which correspond to minor differences between the segmentation matrix and the binary matrix. In this case, it should be estimate if changes are needed.

2.4.2 Modifying the result

The way modifications are applied is very similar to the methods used in commercial 3D analysis software like for example Amira. A resizable brush is controlled via the mouse and used to add or delete voxels to the segmentation. For the modifications a split screen is used. Both screens are locked by slice number, thereby always showing corresponding slices. Adjustments are made on the right screen and the color codes are shown on the left screen, allowing immediate feedback. Voxels that have a value of zero in the original binary matrix, indicating soft tissue and bone, should have no voxels with a value of one in the eventual segmentation results. This comes down to adding new red voxels. Such voxels added during the manual adjustment step will automatically be removed.

3. Results

The results of two runs are given below. For both runs the settings were as follows: a total of 24 iterations were applied; the half-length L of the sample line was 30; γ was set to 1; and the stiffness α ranged from 40 to 4. The b-parameters were limited to 3 standard deviations. Using the ‘parallel pool' feature of Matlab, the calculations were done on 16 cores of an Intel Xeon CPU (E5 2630 v3 2.4 GHz). The color map of the active shape modeling step was created by using the values of the minimal Mahalanobis value along the sample line, as calculated for each landmark. The logarithm of these values was taken and an interpolation was done across the nasal surface. Red and blue indicate a high and low value, respectively. Small light blue squares are superimposed on this color map. These squares indicate the landmarks that contribute to the calculation of the b-parameters. In the beginning only a small percentage of landmarks (those with the lowest Mahalanobis distance) will contribute. With each iteration, this number will steadily increase (as can been seen on the figures below) up until 95 percent in the final iteration.

3.1 Segmentation of a training nose

Figure 9 shows the intermediate results that were obtained during the fitting process of a CT scan corresponding to one of the training shapes of the shape model. On top, the initialization of the shape model (in blue) in the binary matrix (gray) is depicted. At that moment, no iterations of the ASM algorithm have been applied. Subsequently, an ASM step was alternated with an elastic surface deformation, and both results are shown for the 6th, 12th, 18th and 24th (final) iteration.

Because a manual segmentation result is available for this nose, it is possible to have an objective quantification of the segmentation accuracy. In this work, the Dice coefficient (Taha and Hanbury, 2015) was used. The Dice coefficient is defined as:

$$DICE = \frac{2|X \cap Y|}{|X| + |Y|}$$

(eq. 17)

with X and Y two sets of binary data, and $|X|$ and $|Y|$ the number of elements in each set. The coefficient can take any value from 0 to 1. A value of 1 indicates a complete overlap, and 0 indicates no overlap. The value for the Dice coefficient of this fit was 0.869.

3.2 Segmentation of a new nose

The result shown in figure 10 is obtained by applying the fitting procedure on an unseen nose. This is done by leaving one shape out of the shape model training data. The nose that was left out was the same nose used in section 4.1. In this way, both results can be compared in the discussion section. The value obtained for the Dice coefficient was again 0.869.

4. Discussion

4.1 Statistical shape model

Clinical tomographic data is used to calculate the average morphology of the nasal cavity and their variation with a high precision. It is beyond the scope of the present work to analyze in depth how the airway statistical shape model is created. Here, we focus on how this how this model, combined with the active shape modeling algorithm, can be applied for the semi-automatic segmentation of a nasal cavity from CT data. The reader is referred to Huysmans et al. (2010) for further information on the correspondence algorithm.

Geometrical surface models are needed to create a SSM. These models are created by segmentation, which depends to some degree on the operator's subjective input. To avoid inter-operator generated variation in the shape model, all segmentations in this study were done by the same operator.

In this work, the choice was made to cut the training shapes at the floor of the inferior turbinates, in the postnasal region. From these shapes the average shape and the shape modes were calculated, such as shown in figure 7. This choice leads to an extra step in the segmentation process. First the NP needs to be excluded, but later on it has to be included again to obtain the full nasal cavity, with NP. However, this extra step adds only a fractional amount of time to the total process, and defining the shape model like this also has some advantages. The principal components obtained from these training shapes contain more detail about the morphological variation of this part because the considered shape is smaller. Also, because of this choice for the shape of the SSM, an extra surface part at the bottom of the postnasal region is created. This extra part is like a cap that seals the bottom of the back-end of the nasal cavity. When the NP would be included in the shape model, this cap would be positioned much lower. Landmarks on this cap will, just like the other landmarks, contribute during the ASM algorithm. In the beginning of the algorithm, when the shape model is initialized, its shape is still very different from the shape that has to be reconstructed. Only a small part of the landmarks at the back-end will at this time find an appropriate match. Because of this, only a fraction will contribute to the deformation of the shape model. The contribution of these extra landmarks is therefore useful. They pull the shape model towards the cap at the inferior side, while at the same time the landmarks on the superior side pull towards the other side. This combined action causes a stable grow of the back-end, increasing the probability that the other landmarks will also find an appropriate match.

A major advantage of SSM is the small amount of parameters needed to describe the shape variation. Because higher principal components represent small variations, most of the variation can be represented with a limited number of parameters. For the nasal shape model, PC 47 to 95 have a combined contribution of around 5 percent. The active shape modeling algorithm makes optimal use of this parameter reduction during the shape projection step.

The SSM technique used in this work has as disadvantage that all shapes need to have the same topology (genus-0). This is not always the case for every nose (e.g. nasal septum perforation) and is not demanded by every SSM approach, for example level-set based SSMs. However, segmentation differences caused by this can easily be detected and subsequently be manually dealt with.

4.2 Active shape modeling

Another technique comparable to ASM is active appearance modeling (AAM). This algorithm uses a model that represents both variations in shape and in voxel intensity. The model is also trained using labelled images, with landmarks marked on each training object. For more information, the reader is referred to Cootes et al. (1998). In contrast to ASM, updating the current position of a model vertex for an AAM does not use sample lines to search locally around that vertex. Instead it uses the full image data under the current shape instance and looks at the difference between the image sample and a manufactured model sample to update model parameters. In Cootes et al. (1999) the ASM algorithm was compared with the AAM algorithm. They used two data sets: a set of faces and a set of MR brain sections. They report that AAM gives a better match to the image intensity, and that AAMs allow building a convincing model with a relatively small number of landmarks. They also found that ASMs have a larger capture range because they sample around the current position of the vertices. ASM is faster than AAM and achieves more accurate feature point location. The choice was therefore made to use active shape modeling.

In this work, binary appearance was used. This means that a new CT scan first needed to be transformed into a binary matrix. At that point, a watershed transformation was applied as a preprocessing step to already remove a large part of the sinuses. This allowed a better estimate of the centroid for the initialization of the shape model, which also significantly lowers the probability that during fitting the shape model tries to fit to a wrong structure. This binary approach has a major benefit: all the subsequent steps in the toolbox (coarse and fine segmentation) are independent of data modality. This means that in principle CT, CBCT and MRI should make no difference and the toolbox should be able to process data coming from the different imaging techniques. However, further testing on all data modalities has to be done and evaluated to confirm this statement. With respect to MRI data, this will largely depend on the quality of the delineation of the boundaries of the nasal cavity and sinuses, such that it is possible to define a region of interest. For MRI scans, this delineation can be poor.

The fine segmentation allowed excluding those parts of the sinuses that remained after the coarse segmentation. In this way, the paranasal sinuses are totally excluded from the nasal cavity.

4.3 Voxelization

After the fine segmentation step, the resulting mesh is voxelized. This allows making changes to the segmentation result on the basis of prior knowledge. For example, when a septal perforation is present in the original data or an occlusion is not fitted well by the ASM, it can easily be adjusted on the basis of anatomic insight. Comparing the result with the original tomographic data is also straightforward. However, the voxelization step itself can have an influence on the segmentation result. An objective estimate to quantify this influence is not that trivial when one wants to start from an instance of the shape model (triangular surface mesh). For example, starting from the average nasal cavity, a voxelization step can be applied. Without any editing, the reverse step is taken and one again ends up with a triangular surface mesh of the nasal cavity. However, the generated triangular surface does not need to have the same amount of vertices and those vertices do not have to be on the same anatomical position. Using a sum of squares as a measure for the difference between the vertices of the initial average nose and the one obtained after the two steps is not possible without first applying a correspondence step. This correspondence step can have its own influence, hereby having a confounding effect on the value obtained for the influence. The choice was therefore made to make an estimate using the Dice coefficient. A surface mesh is generated, and subsequently voxelization is applied. Results were obtained for a simple sphere at different grid resolutions (40^3, 80^3, 160^3). This gave an almost constant Dice coefficient 0.924, which is a rather low value given the simplicity of the considered object. Improving this algorithm in the future may yield a significant increase in the accuracy of the segmentation matrix.

When the segmentation is part of a CFD analysis, the final format is often a 3D surface mesh of the nose. In this case, after the manual step, a surface generation step is needed. The process of surface generation can also have an effect on the result, but this is non-specific to the approach of this work and is exactly the same in the case of a complete manual segmentation.

4.4 Other work

As was mentioned in the introduction, other methods exist to perform segmentation of the upper respiratory tract. In the following, those which relate the most to the presented work are discussed.

Last et al. (2010) applied a data-based shape model based on a parametric level set. They aimed to segment the combination of the nasal cavity and paranasal sinus boundaries, because these are the critical structures in robot assisted functional endoscopic sinus surgery (RAFESS). They report great performance in the segmentation of the overall shape of nasal cavity, maxillary and ethmoidal sinuses. For the construction of their deformable shape model they also used hand-segmented 3D CT data. However, their method concentrates on segmenting the nasal structures one 2D slice at a time. Such an approach inherently has a higher probability of sharp local jumps in the combined 3D result. For RAFESS this will probably not pose an issue, but the result of the same slice-wise approach for sole segmentation of the nasal cavity would be less appropriate for e.g. CFD calculations.

Bui et al. (2015) also used level set segmentation. A coarse-to-fine multilevel procedure was created to construct the nasal cavity together with paranasal sinuses from CBCT data. In comparison to the semi-automatic approach presented in the current paper (where user interaction is required during the coarse steps and shape initialization), the approach of Bui et al., does not require manual interaction. Gaussian mixture model thresholding and morphological operators are used to automatically locate the region of interest and to initialize the active contour. This fully automatic approach has some advantages and should be taken into consideration for further developments.

In Huang et al. (2016) it is put forward that methods using prior knowledge, for example a shape or appearance model, perform better because they are able to detect the narrower airway passages within the nasal cavity. They also made use of a shape model, but in combination with a locally constrained random walk algorithm. However, in their work the shape model was constructed using level sets. Level sets have some known weaknesses. For example, gaps in a boundary can cause the evolving contour to leak through these gaps. Objects with incomplete contours therefore have the chance to be identified only partially and/or incorrectly. Other common problems in level sets are so called shocks, which can arise in level sets and cause problems like orientation discontinuity (Suri et al., 2002). A CPU implemented level set method can also be very slow when working with big 3D data volumes.

A free upper respiratory tract 3D model reconstruction software, called NASAL-Geom, was described in Cercos-Pita et al. (2018), which was optimized for producing 3D nasal geometries from CT scans. In NASAL-geom, the reconstruction process is a combination of morphological operations; no prior knowledge of for example shape is used. The software consists of three stages: preprocessing the images, nasal cavity segmentation and constructing the 3D geometry. A sequence of filter operations and transformations is applied on the image data before these are used to extract the voxels representing the air. A combination of a 3D and 2D watershed algorithm is used for this, followed by a nostril refinement step. The final stage is based on the Marching Cubes Algorithm (Lorensen and Cline, 1987), polygon decimation and smoothing. The software is open source. In the longer term, it is also the intention to make the current Matlab toolbox open source, which will expedite further development.

In contrast, “Mecomland”, discussed in Burgos et al. (2017), is a paid product of ServiMeCom (Computational Medical Services). In their work, they report as a main contribution the development of a novel interpolation algorithm to build a 3D model from the label files. They report that this is better suited for the complex nasal geometry than the Marching Cubes Algorithm.

4.5 Future directions

In the near future it is intended to increase the amount of nasal training shapes. This will have a positive effect on the nasal variation captured by the statistical shape model, which will further increase the probability that an unseen nose falls within the known shape space. It will increase the robustness and accuracy of the algorithm. Because of this, the manual intervention time that is needed at post processing will shorten, until eventually a point is reached where (almost) no post-processing is needed. A situation in which a newly segmented nasal cavity automatically becomes a new training shape for the SSM is preferable. An online portal providing access to the tool would be an optimal method for this, as it would allow centralized data gathering and supervision. Periodical updates of the SSM can then be made for everyone to benefit from. Before such a portal can be achieved, a robustness and accuracy baseline has to be reached.

Different approaches for the shape models have to be tested in the future, i.e. if segmentation using a multi-SSM approach (e.g. one SSM for each sex or age group) gives better results than one SSM trained on all shapes. The former demands that all collected shape data is divided into classes in function of demographics.

A first good future addition to the toolbox would be the option to include a part of the outer face to the segmentation domain. This makes it possible to define a highly realistic boundary condition at the nostrils during the CFD calculations. A second improvement to the current version would be the option for the user to exclude/include the sinuses to the domain after the segmentation refinement step.

Another point of work is the voxelization algorithm, as observed by applying it on a simple shape. Improving this will contribute to an increase in segmentation accuracy.

Adding quality measures to the toolbox would also be an upgrade. For example, measures that quantitatively describe how good the boundary of the chosen mask is fitted by the shape model at each iteration. Currently, the exact amount of fitting iterations at which the algorithm is stopped is determined by the user. Developments towards a more automatic manner based on user defined conditions, like for example the quality of fit or the maximum number of iterations/maximum fitting time would be an improvement.

5. Conclusion

The obtained results demonstrated that the approach presented in this work can be used for the semi-automatic segmentation of a human nasal cavity from tomographic data, which substantially reduces the amount of operator time. The value for the Dice coefficient (0.869) indicates that for now, some small manual changes at the end are preferable. One set of nasal data was left out of the training data and the fitting procedure was applied to the corresponding CT scan. Comparing the Dice coefficient to the one with the nose included in the training data (both were equal), showed that the technique looks promising in terms of generalization (how well the shape model fits new unseen noses). There is however still room for improvement.

References

Alsufyani, N. A., Hess, A., Noga, M., Ray, N., Al-Saleh, M. A. Q., Lagravère, M. O., Major, P. W., 2016. New algorithm for semiautomatic segmentation of nasal cavity and pharyngeal airway in comparison with manual segmentation using cone-beam computed tomography. Am J Orthod Dentofacial Orthop. 150, 703-712.

Amberg, B., Romdhani, S., Vetter, T., 2007. Optimal Step Nonrigid ICP Algorithms for Surface Registration. IEEE Comput Soc Conf Comput Vis Pattern Recognit. 1-8.

Bui, N. L., Ong, S. H., Foong, K. W., 2015. Automatic segmentation of the nasal cavity and paranasal sinuses from cone-beam CT images. Int J Comput Assist Radiol Surg. 10, 1269-1277.

Burgos, M. A., Sanmiguel-Rojas, E., Del Pino, C., Sevilla-Garcia, M. A., Esteban-Ortega, F., 2017. New CFD tools to evaluate nasal airflow. Eur Arch Otorhinolaryngol. 274, 3121-3128.

Cercos-Pita, J. L., Cal, I. R., Duque, D., de Moreta, G. S., 2018. NASAL-Geom, a free upper respiratory tract 3D model reconstruction software. Comput Phys Commun. 223, 55-68.

Cootes, T. F., Taylor, C. J., Cooper, D. H., Graham, J., 1995. Active Shape Models-Their Training and Application. Comput Vis Image Underst. 61, 38-59.

Cootes, T. F., Edwards, G. J., Taylor, C. J., 1998. Active appearance models. Comput Vis ECCV. 484-498.

Cootes, T. F., J. Edwards, G., Taylor, C., 1999. Comparing Active Shape Models with Active Appearance Models. BMVC.

Dastidar, P., Heinonen, T., Numminen, J., Rautiainen, M., Laasonen, E., 1999. Semi-automatic segmentation of computed tomographic images in volumetric estimation of nasal airway. Eur Arch Otorhinolaryngol. 256, 192-198.

Davies, R. H., Twining, C. J., Cootes, T. F., Waterton, J. C., Taylor, C. J., 2002. A minimum description length approach to statistical shape modeling. IEEE Trans Med Imaging. 21, 525-537.

Di, M.-Y., Jiang, Z., Gao, Z.-Q., Li, Z., An, Y.-R., Lv, W., 2013. Numerical Simulation of Airflow Fields in Two Typical Nasal Structures of Empty Nose Syndrome: A Computational Fluid Dynamics Study. PLOS ONE. 8, e84243.

Doorly, D. J., Taylor, D. J., Schroter, R. C., 2008. Mechanics of airflow in the human nasal airways. Respir Physiol Neurobiol. 163, 100-110.

El, A. S., El, H., Palomo, J. M., Baur, D. A., 2011. A 3-dimensional airway analysis of an obstructive sleep apnea surgical correction with cone beam computed tomography. J Oral Maxillofac Surg. 69, 2424-2436.

Frank-Ito, D. O., Kimbell, J. S., Laud, P., Garcia, G. J., Rhee, J. S., 2014. Predicting postsurgery nasal physiology with computational modeling: current challenges and limitations. Otolaryngol Head Neck Surg. 151, 751-759.

Garcia, G. J., Bailie, N., Martins, D. A., Kimbell, J. S., 2007. Atrophic rhinitis: a CFD study of air conditioning in the nasal cavity. J Appl Physiol. 103, 1082-1092.

Garcia, G. J., Schroeter, J. D., Segal, R. A., Stanek, J., Foureman, G. L., Kimbell, J. S., 2009. Dosimetry of nasal uptake of water-soluble and reactive gases: a first study of interhuman variability. Inhal Toxicol. 21, 607-618.

Grant, O., Bailie, N., Watterson, J., Cole, J., Gallagher, G., Hanna, B., 2004. Numerical model of a nasal septal perforation. Stud Health Technol Inform. 107, 1352-1356.

Huang, R., Li, A., Bi, L., Li, C., Young, P., King, G., Feng, D. D., Kim, J., 2016. A locally constrained statistical shape model for robust nasal cavity segmentation in computed tomography. IEEE Int Symp Biomed Imaging . 1334-1337.

Huysmans, T., Sijbers, J., Verdonk, B., 2004. Parameterization of Tubular Surfaces on the Cylinder Journal of WSCG. 13, 97-104.

Huysmans, T., Sijbers, J., Verdonk, B., 2010. Automatic construction of correspondences for tubular surfaces. IEEE Trans Pattern Anal Mach Intell. 32, 636-651.

Inthavong, K., Tian, Z. F., Li, H. F., Tu, J. Y., Yang, W., Xue, C. L., Li, C. G., 2006. A Numerical Study of Spray Particle Deposition in a Human Nasal Cavity. Aerosol Sci Technol.. 40, 1034-1045.

Inthavong, K., Ma, J., Shang, Y., Dong, J., Chetty, A. S. R., Tu, J., Frank-Ito, D., 2017. Geometry and airflow dynamics analysis in the nasal cavity during inhalation. Clin Biomech, in press.

Iwasaki, T., Saitoh, I., Takemoto, Y., Inada, E., Kanomi, R., Hayasaki, H., Yamasaki, Y., 2011. Evaluation of upper airway obstruction in Class II children with fluid-mechanical simulation. Am J Orthod Dentofacial Orthop. 139, 135-145.

Jeter, M. W., 1986. Mathematical Programming: An Introduction to Optimization. M Dekker, Inc, USA.

Karakosta, P., Alexopoulos, A. H., Kiparissides, C., 2015. Computational model of particle deposition in the nasal cavity under steady and dynamic flow. Comput Methods Biomech Biomed Engin. 18, 514-526.

Keyhani, K., Scherer, P. W., Mozell, M. M., 1995. Numerical simulation of airflow in the human nasal cavity. J Biomech Eng. 117, 429-441.

Keyhani, K., Scherer, P. W., Mozell, M. M., 1997. A numerical model of nasal odorant transport for the analysis of human olfaction. J Theor Biol. 186, 279-301.

Kimbell, J. S., Segal, R. A., Asgharian, B., Wong, B. A., Schroeter, J. D., Southall, J. P., Dickens, C. J., Brace, G., Miller, F. W., 2007. Characterization of deposition from nasal spray devices using a computational fluid dynamics model of the human nasal passages. J Aerosol Med. 20, 59-74.

Last, C., Winkelbach, S., Wahl, F. M., Eichhorn, K. W. G., Bootz, F., 2010. A Model-Based Approach to the Segmentation of Nasal Cavity and Paranasal Sinus Boundaries. Pattern Recognit. 333-342.

Leong, S. C., Chen, X. B., Lee, H. P., Wang, D. Y., 2010. A review of the implications of computational fluid dynamic studies on nasal airflow and physiology. Rhinology. 48, 139-145.

Lindemann, J., Brambs, H. J., Keck, T., Wiesmiller, K. M., Rettinger, G., Pless, D., 2005. Numerical simulation of intranasal airflow after radical sinus surgery. Am J Otolaryngol. 26, 175-180.

Lindemann, J., Rettinger, G., Kroger, R., Sommer, F., 2013. Numerical simulation of airflow patterns in nose models with differently localized septal perforations. Laryngoscope. 123, 2085-2089.

Lorensen, W. E., Cline, H. E., 1987. Marching cubes: A high resolution 3D surface construction algorithm. J SIGGRAPH Comput. Graph. 21, 163-169.

Ozlugedik, S., Nakiboglu, G., Sert, C., Elhan, A., Tonuk, E., Akyar, S., Tekdemir, I., 2008. Numerical study of the aerodynamic effects of septoplasty and partial lateral turbinectomy. Laryngoscope. 118, 330-334.

Rhee, J. S., Book, D. T., Burzynski, M., Smith, T. L., 2003. Quality of life assessment in nasal airway obstruction. Laryngoscope. 113, 1118-1122.

Rhee, J. S., Pawar, S. S., Garcia, G. J. M., Kimbell, J. S., 2011. Towards Personalized Nasal Surgery Using Computational Fluid Dynamics. Arch Facial Plast Surg. 13, 305-310.

Schroeter, J. D., Kimbell, J. S., Asgharian, B., 2006. Analysis of particle deposition in the turbinate and olfactory regions using a human nasal computational fluid dynamics model. J Aerosol Med. 19, 301-313.

Seo, A., Chung, S. K., Lee, J., Kim, J., Kim, H., 2010. Semiautomatic Segmentation of Nasal Airway Based on Collaborative Environment. ISUVR. 56-59.

Shi, H., Scarfe, W. C., Farman, A. G., 2006. Upper airway segmentation and dimensions estimation from cone-beam CT image datasets. Int J Comput Assist Radiol Surg. 1, 177-186.

Subramaniam, R. P., Richardson, R. B., Morgan, K. T., Kimbell, J. S., Guilmette, R. A., 1998. Computational fluid dynamics simulations of inspiratory airflow in the human nose and nasopharynx. Inhal Toxicol. 10, 91-120.

Suri, J., Liu, L., Singh, S., Laxminarayan, S., Zeng, X., Reden, L., 2002. Shape recovery algorithms using levels sets in 2-D/3-D Medical Imagery: A state-of-the-art review. IEEE Trans Inf Technol Biomed. 6, 8-28.

Taha, A. A., Hanbury, A., 2015. Metrics for evaluating 3D medical image segmentation: analysis, selection, and tool. BMC Med Imaging. 15, 29.

Taubin, G., 1995. Curve and surface smoothing without shrinkage. Proc IEEE fifth Int Conf Comput Vis. 852-857.

Thodberg, H.H., 2003. Minimum description length shape and appearance models. Inf Process Med Imaging. 51-62.

Tingelhoff, K., Moral, A. I., Kunkel, M. E., Rilk, M., Wagner, I., Eichhorn, K. W. G., Wahl, F. M., Bootz, F., 2007. Comparison between Manual and Semi-automatic Segmentation of Nasal Cavity and Paranasal Sinuses from CT Images. Conf of the IEEE EMBS. 5505-5508.

Wen, J., Inthavong, K., Tu, J., Wang, S., 2008. Numerical simulations for detailed airflow dynamics in a human nasal cavity. Respir Physiol Neurobiol. 161, 125-135.

Wexler, D., Segal, R., Kimbell, J., 2005. Aerodynamic effects of inferior turbinate reduction: computational fluid dynamics simulation. Arch Otolaryngol Head Neck Surg. 131, 1102-1107.

Xiong, G. X., Zhan, J. M., Jiang, H. Y., Li, J. F., Rong, L. W., Xu, G., 2008. Computational fluid dynamics simulation of airflow in the normal nasal cavity and paranasal sinuses. Am J Rhinol. 22, 477-482.

Mesh voxelization, 2013. Mesh voxelization package from Matlab central file exchange website. https://nl.mathworks.com/matlabcentral/fileexchange/27390-mesh-voxelisation (last accessed 16 August 2018)

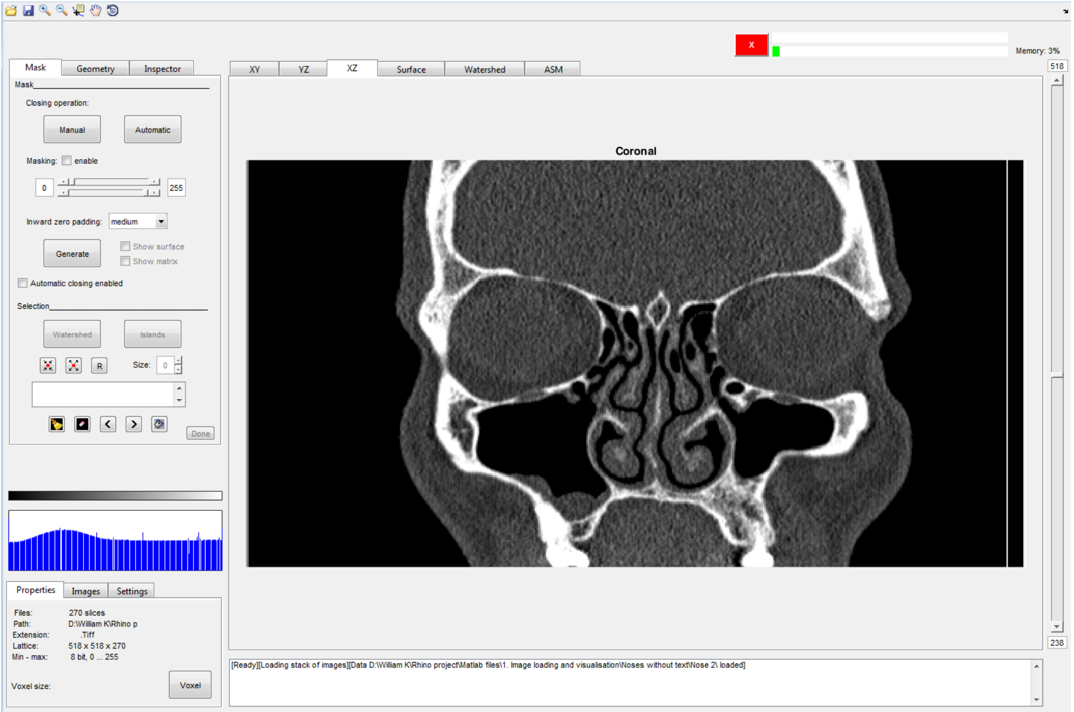

Files: 270 slices
Path: D:\William K\Rhino p
Extension: .Tiff
Lattice: 518 x 518 x 270
Min - max: 8 bit, 0 ... 255

```
[Ready][Loading stack of images][Data D:\William K\Rhino project\Matlab files\1. Image loading and visualisation\Noses without text\Nose 2\ loaded]
```

Figure 1: general view of the user interface. On the top left, by clicking on the tab names, the tabs belonging to the three different steps become visible. When CT data is loaded into the toolbox, a grayscale histogram is shown and information appears in the 'properties' tab. The first three view tabs (located on top of the main

window) in combination with the slider allow choosing a transversal, sagittal or coronal slice respectively. Clicking on one of the last three tabs shows the different intermediate results (if already obtained). In the bottom tab, short information or error messages are displayed.

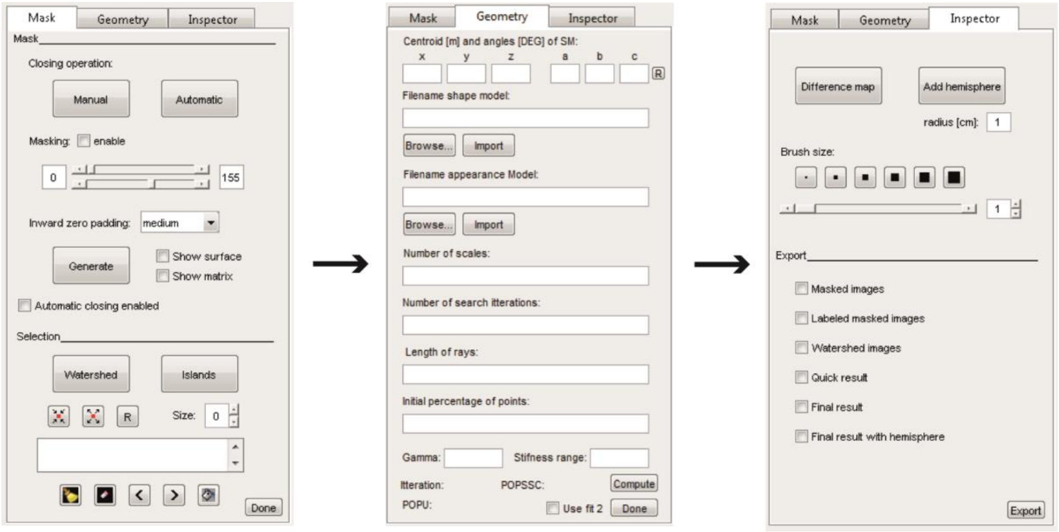

Masking: 0 – 155

Inward zero padding: medium

Size: 0

radius [cm]: 1

Figure 2: detailed view of the three main tabs used during the fitting process. From left to right, the 'mask', 'geometry' and 'inspector' tab are shown, respectively. The first two tabs constitute the steps that have to be taken to go from the original CT data to a segmented result. The last tab allows the inspection of the segmentation result and manual adjustments.

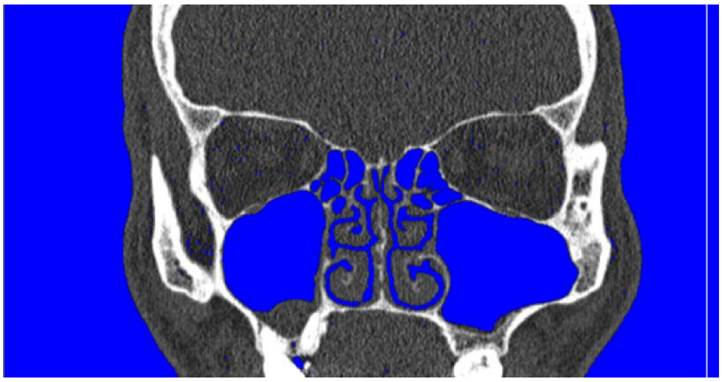

Figure 3: example of a coronal slice of the human head. A user can determine the grayscales of interest by choosing the lower and upper limit. During this step, the voxels belonging to the region of interest are indicated in blue, providing an immediate visual feedback while changing the limits.

755 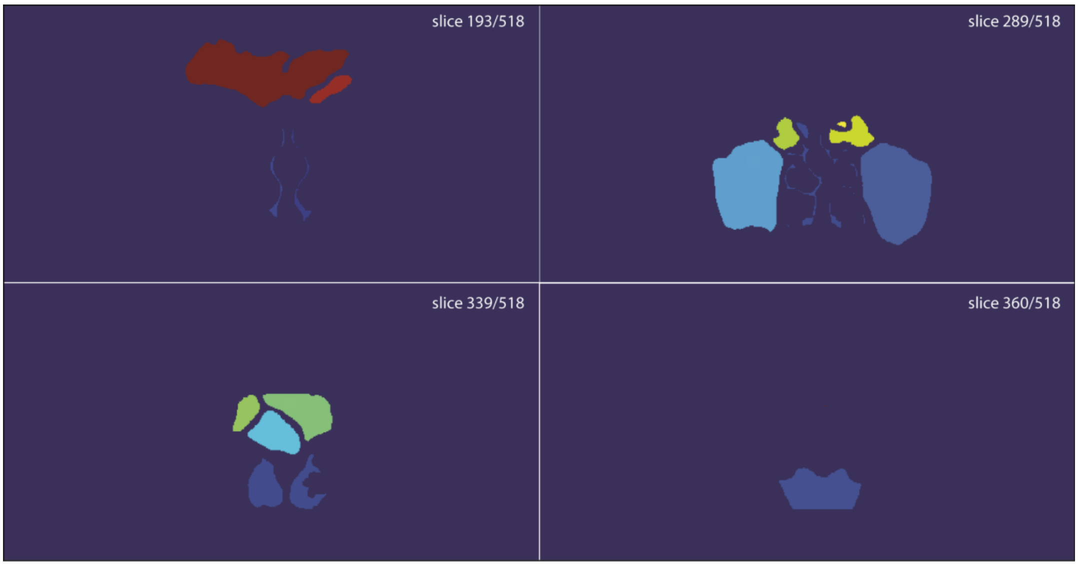

Figure 4: coronal slices after the watershed procedure at different scan positions. The user can click on the (visually separated) parts to remove them. When a region is clicked in one coronal slice, the complete 3D part is removed from the matrix.

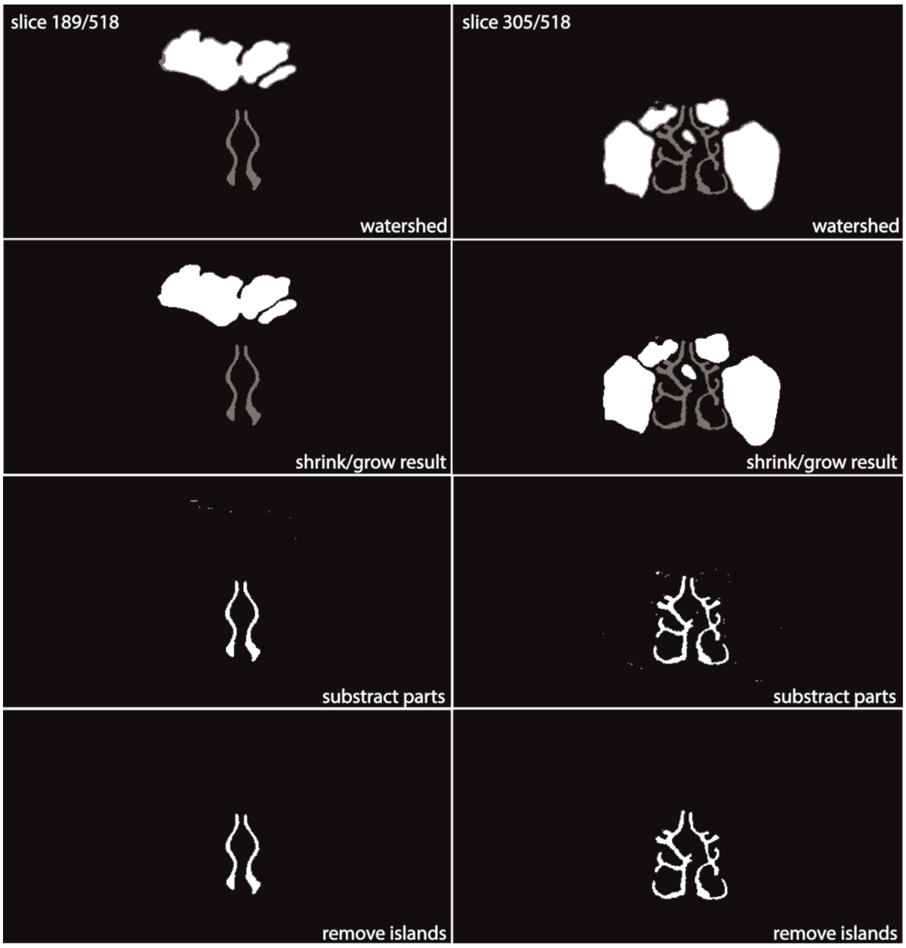

Figure 5: coronal slices for two scan positions at different steps in the coarse segmentation procedure. The top images show the original binary matrix overlain with the watershed parts that were indicated by the user in the previous step. These parts were then grown in size and subtracted from the binary matrix. As a final step, small clusters of voxels created by the subtraction, called islands, were removed.

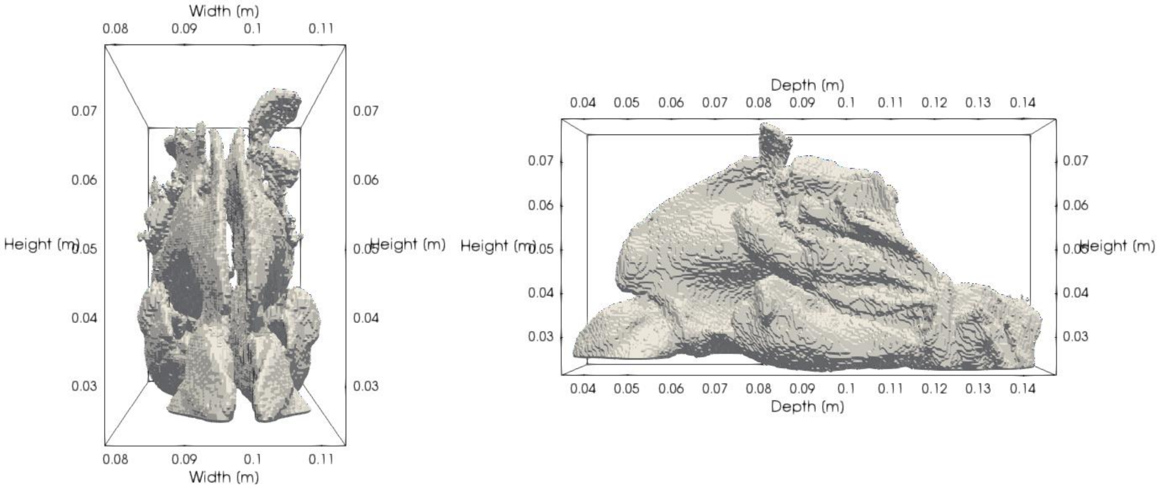

Figure 6: example of a surface model created from binary data in the coarse segmentation step. It is clear that almost all sinuses are removed, but that the current geometry still contains some unwanted parts. This geometry will become the simulation domain in a later step, so these have to be removed.

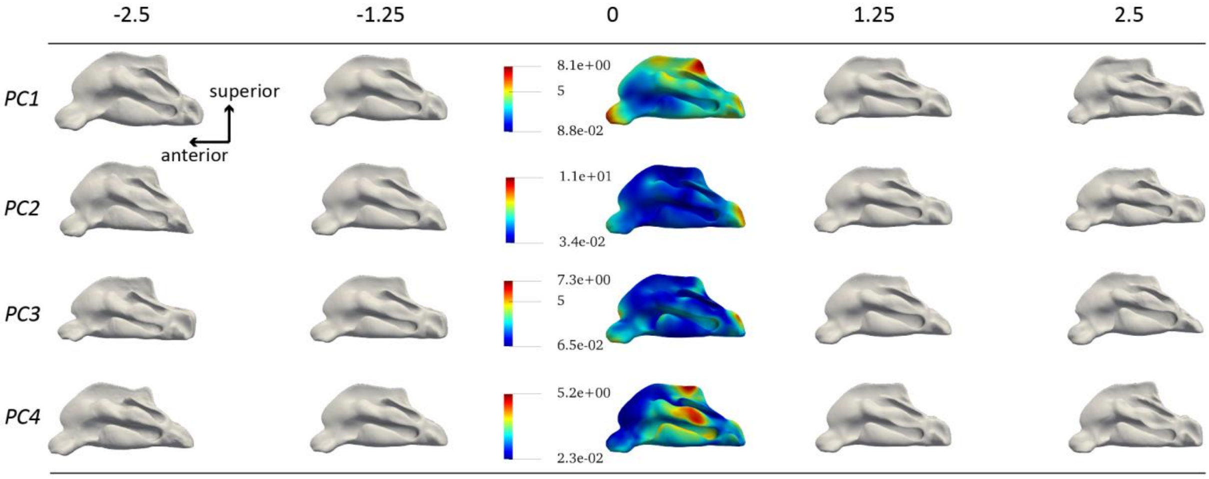

Figure 7: first four shape modes of the SSM. They are obtained by applying the principal components to the average shape for different multiples of the standard deviation [-2.5 – 2.5]. The color map represents the magnitude (in mm) of variation for the i^{th} principal component.

Figure 8: example of a visual map of the goodness of fit. The nasal cavity is blue and the sinuses are green. Scattered around the nasal cavity some red voxels can be found, which correspond to minor differences between the segmentation matrix and the binary matrix. A map such as the one shown here corresponds to a quasi-perfect segmentation (for this slice).

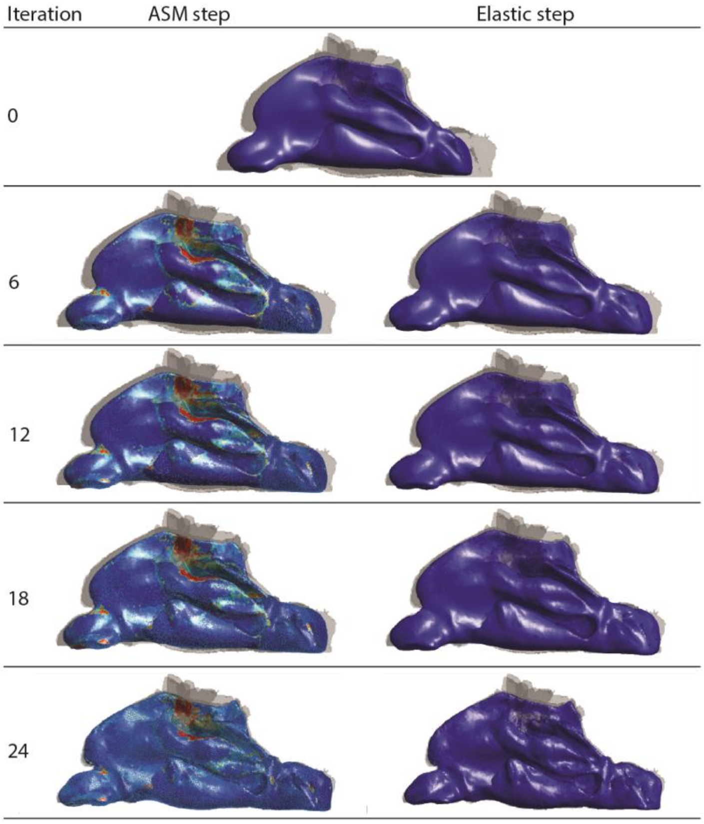

Figure 9: intermediate results when fitting to a training shape of the shape model. On top, the initialization of the shape model (in blue) in the binary matrix (gray) is depicted. Intermediate results are shown for the ASM

and the elastic step at four moments in the fitting process. The color map of the ASM step represents the minimal Mahalanobis value. The logarithm of the value at each landmark was taken and an interpolation was done across the nasal surface. Red and blue indicate a high and low value, respectively. Light blue squares superimposed onto this color map indicate the landmarks that contribute to the calculation of the b-parameters.

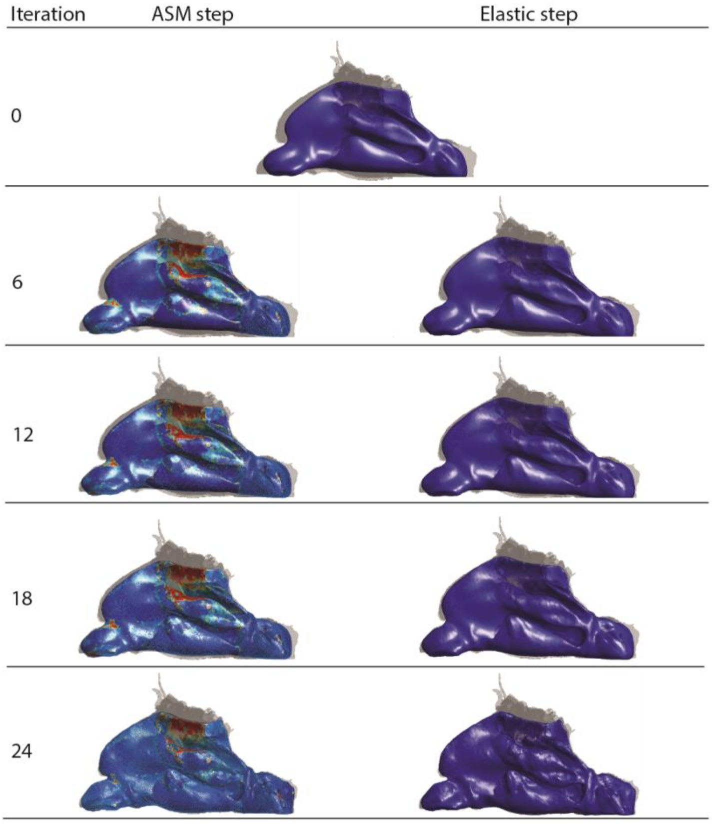

Figure 10: intermediate results when fitting to an unknown shape (leave-one-out). On top, the initialization of the shape model (in blue) in the binary matrix (gray) is depicted. Intermediate results are shown for the ASM and the elastic step at four moments in the fitting process. The color map of the ASM step represents the minimal Mahalanobis value. The logarithm of the value at each landmark was taken and an interpolation was done across the nasal surface. Red and blue indicate a high and low value, respectively. Light blue squares superimposed onto this color map indicate the landmarks that contribute to the calculation of the b-parameters.